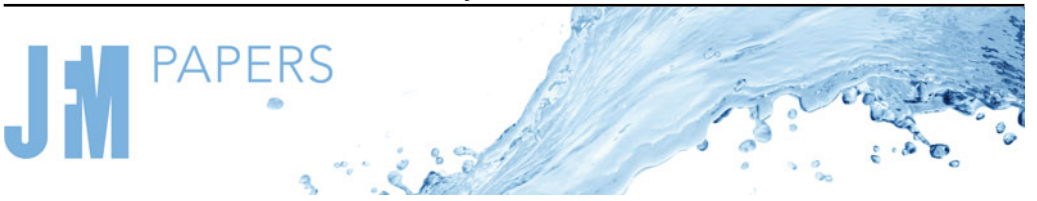
J. Fluid Mech. (2026), *vol.* 1034, A57, doi:10.1017/jfm.2026.11512



Strong-shock-driven Richtmyer–Meshkov instability at quasi-single-mode interfaces

Wei Cai[1], **He Wang**[1] **and Ting Si**[1]

[1]State Key Laboratory of High-Temperature Gas Dynamics, School of Engineering Sciences, University of Science and Technology of China, Hefei 230026, PR China

Corresponding author: He Wang, ustchewang@ustc.edu.cn

(Received 11 November 2025; revised 26 February 2026; accepted 2 April 2026)

Richtmyer–Meshkov instability (RMI) at quasi-single-mode interfaces subjected to strong shocks with Mach number exceeding 3.0 is investigated through shock-tube experiments. To reveal the influence of higher-order initial modes, one single-mode and four quasi-single-mode interfaces with varying modal compositions are examined. The Richtmyer theory is experimentally verified for the first time to accurately capture the single-mode interface evolution from start-up to the linear stage. In contrast, it fails for quasi-single-mode scenarios, highlighting the significant effect of higher-order modes. By incorporating the influence of higher-order modes via linear superposition, a linear model for quasi-single-mode interface evolution is proposed, whose validation indicates negligible modal coupling in early evolution. For the nonlinear period, a representative model for weak-shock-driven RMI at a single-mode interface performs poorly, as it does not consider the influence of higher-order modes and key mechanisms such as shock proximity, secondary compression and spike acceleration. Based on the present findings, an empirical nonlinear model with favourable predictive capability is developed. Furthermore, by matching the new linear and nonlinear models, a complete description of the amplitude evolution of single-mode and quasi-single-mode interfaces from start-up to nonlinear stages is achieved, offering new insight into modelling strong-shock-driven RMI.

Key words: shock waves, gas dynamics

1. Introduction

Richtmyer–Meshkov instability (RMI) (Richtmyer 1960; Meshkov 1969) is a fundamental hydrodynamic instability that arises when a shock wave interacts with a perturbed interface separating two fluids with distinct densities. During the RMI evolution, the lighter fluid

© The Author(s), 2026. Published by Cambridge University Press.

https://doi.org/10.1017/jfm.2026.11512 Published online by Cambridge University Press

penetrates into the heavier fluid, forming bubble structures, while the heavier fluid intrudes into the lighter fluid, forming spike structures. As a foundation for RMI research, the instability on single-mode interfaces (single-mode RMI) has been the subject of extensive investigation (Brouillette 2002; Zhou 2017*a*,*b*, 2024; Zhou *et al.* 2021). However, in engineering applications and natural phenomena involving RMI, such as inertial confinement fusion (ICF) (Zhou, Sadler & Hurricane 2025) and supernova explosions (Abarzhi *et al.* 2019), the instability is typically seeded by stochastic perturbations at material interfaces. Therefore, investigating the instability on multi-mode interfaces and elucidating the underlying mechanisms are crucial. Current studies of RMI on broadband or randomly perturbed interfaces predominantly rely on statistical methods to analyse spectral features associated with energy transfer (Dimonte *et al.* 2024; Zhou 2024; Zhao *et al.* 2025). The inherent complexity of the initial perturbation spectrum in such configurations hinders elucidating the influence of higher-order initial modes on interface evolution (higher-order-mode effect). This challenge highlights the necessity for research into simpler interface configurations. Quasi-single-mode interfaces possess a dominant mode that preserves geometric regularity while simultaneously incorporating higher-order components. This feature makes the RMI at quasi-single-mode interfaces (quasi-single-mode RMI) a critical bridge connecting classical single-mode RMI and RMI on interfaces with stochastic perturbations, and a favourable subject for exploring the higher-order-mode effect on interface evolution.

Extensive experimental efforts have been devoted to examining the RMI on specific types of quasi-single-mode interfaces, with particular emphasis on the V-shaped interface evolution (Rikanati *et al.* 2003; Reilly *et al.* 2015; Luo *et al.* 2016; Mohaghar *et al.* 2017, 2019; Guo *et al.* 2019). However, these studies primarily concerned the dependence of quasi-single-mode RMI on parameters such as the initial amplitude and shock strength, without exploring the higher-order-mode effect. To investigate the influence of higher-order initial modes, Bakhrakh *et al.* (1995) studied RMI at circular-arc, square-waveform and V-shaped interfaces subjected to a shock wave with Mach number $M_s = 1.44$, combining experimental and numerical approaches. They identified a strong correlation between the amplitude growth and the interface geometry. Liang *et al.* (2019) further examined RMI on diverse quasi-single-mode interfaces, including circular-arc, V-shaped, trapezoidal and square-waveform geometries, accelerated by a shock with $M_s = 1.2$. They demonstrated that the linear evolution of quasi-single-mode RMI differs from that of the single-mode case, with the deviation primarily governed by the Fourier expansion coefficient of the fundamental mode. Additionally, they developed an empirical nonlinear model based on the principle of linear superposition (Mikaelian 2005), which successfully reproduces the weakly nonlinear evolution of all the examined interfaces. Guo *et al.* (2022) conducted experiments on RMI at single-mode, trapezoidal and V-shaped interfaces driven by a weak shock with $M_s = 1.3$. They reported that the growth of the mixing width is strongly dependent on the initial interface profile. Specifically, the higher-order modes of the V-shaped interface are all in phase with the fundamental mode, and their contribution leads the V-shaped interface to evolve more rapidly than the others.

Notably, the experimental studies discussed above were performed exclusively in the weak-shock regime ($M_s < 2.0$). However, in realistic scenarios such as ICF and supernova explosions, RMI is triggered by strong shock waves, which introduce significant compressibility, leading to an evolution law that markedly differs from that under weak-shock conditions (Zhou 2024; Si *et al.* 2025). Consequently, the investigation of strong-shock-induced RMI is of considerable significance. While laser-driven experiments are capable of generating shock waves with M_s up to 10 or even higher (Dimonte & Remington 1993; Dimonte *et al.* 1996; Glendinning *et al.* 2003), they typically involve

https://doi.org/10.1017/jfm.2026.11512 Published online by Cambridge University Press

additional physicochemical processes such as material phase transitions and rarefaction-wave-induced decompression, which complicates isolating the contribution of RMI to perturbation growth. In contrast, shock-tube experiments offer a more controlled and simple physical environment for exploring the RMI dynamics. However, only a few shock-tube experiments on RMI with $M_s \geqslant 2.0$ have been reported (Ranjan *et al.* 2005, 2007), primarily due to the difficulty in generating well-controlled strong shock waves in a shock-tube facility. To our knowledge, the only reported experiment on quasi-single-mode RMI with $M_s \geqslant 2.0$ was conducted by Sadot *et al.* (2003). They employed a solid membrane with a support structure to separate gases, and investigated RMI at a V-shaped interface accelerated by a shock wave with $M_s = 2.0$ in a horizontal shock tube. Their results showed that the amplitude growth is inhibited under the influence of shock proximity and secondary compression. However, the support structure and membrane remnants could exert a significant influence on the perturbation evolution. Moreover, only a single interface configuration was considered, hindering the exploration of the higher-order-mode effect.

To date, desirable and systematic experimental research on quasi-single-mode RMI induced by strong shock waves remains lacking. The underlying evolution mechanisms, along with the applicability of existing models for instability characterisation, are unclear, motivating the present study. In our recent work (Jiang *et al.* 2024), a shock-tube facility capable of producing shock waves with $M_s > 3.0$ while maintaining a 'clean' experimental flow was developed. Furthermore, a novel technique enabling the controllable generation of interfaces without support structures was proposed. These advancements offer a rare opportunity to explore the higher-order-mode effect under strong-shock conditions. In this work, one single-mode interface and four quasi-single-mode interfaces of varying initial modal compositions, including circular-arc, V-shaped, trapezoidal and square-waveform configurations, are considered to highlight the higher-order-mode effect. The morphological evolution of diverse interfaces is first discussed, followed by an analysis of their amplitude evolution dynamics.

2. Experimental methods and set-up

Given the pronounced sensitivity of RMI to initial conditions (Zhou 2024), a high-confidence experimental investigation of strong-shock-driven quasi-single-mode RMI necessitates two essential prerequisites: the generation of a high-intensity shock with a 'clean' post-shock flow field, and the formation of well-controlled initial interfaces.

In the present study, the incident shock with $M_s > 3.0$ and a 'clean' post-shock flow is generated using a recently developed shock-tube facility (Jiang *et al.* 2024), the overall structure of which is illustrated in figure 1. The fundamental principle underlying this facility is that the shock intensity increases as the shock area decreases (Chester 1954; Chisnell 1957; Whitham 1957). The reduction in shock area is achieved through a convergence section specifically designed based on the geometrical shock dynamics (GSD) (Han & Yin 1993; Zhai *et al.* 2010; Zhan *et al.* 2018). During the convergence process, the cross-sectional area of the shock wave decreases from 120 mm × 262 mm to 120 mm × 8 mm, leading to an increase in M_s from approximately 2.0 to over 3.0. In contrast to direct or abrupt shock-contraction approaches, which typically induce strong post-shock disturbances due to shock reflections (Russell 1967), or empirical wall-profile design methods, which demand multiple iterations yet still fail to completely eliminate strong post-shock disturbances (Dowse & Skews 2014), the GSD-based design is capable of producing a stable shock accompanied by a 'clean' post-shock flow.

https://doi.org/10.1017/jfm.2026.11512 Published online by Cambridge University Press

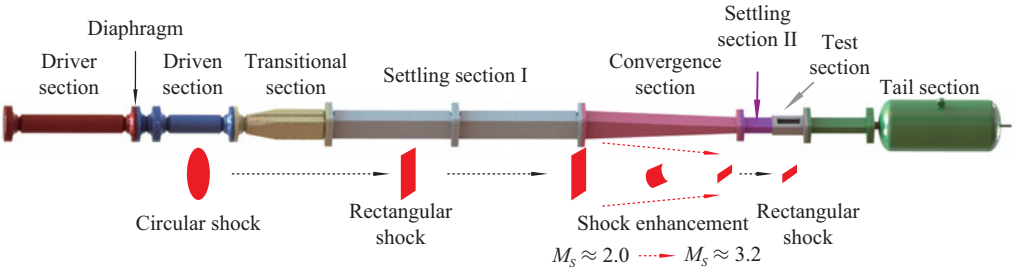


Figure 1. Sketch of the shock-tube facility capable of generating a planar shock with $M_s > 3.0$ while maintaining a 'clean' flow field.

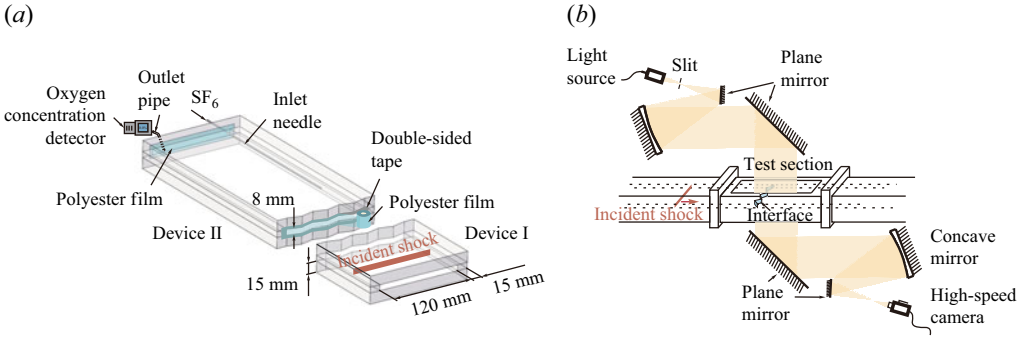


Figure 2. Schematics of (*a*) interface formation method and (*b*) high-speed shadowgraph imaging system.

The initial interfaces are generated using the polyester-film technique developed specifically for strong-shock-driven RMI experiments (Jiang *et al.* 2024; Cai *et al.* 2025; Si *et al.* 2025). The interface-formation devices (I and II), shown in figure 2(*a*), are fabricated by assembling transparent acrylic plates and pedestals, with the adjacent boundaries machined into the desired interface profile. The procedure for interface formation is as follows. Polyester films with thickness 2 μm are first carefully attached to the upstream and downstream sides of device II using double-sided tape. To enable gas replacement in device II, two small holes are punctured in the downstream film, allowing the insertion of an inlet needle and an outlet pipe. Then SF_6 is injected through the inlet, while air is vented through the outlet. The exhausted gas is monitored using an oxygen concentration detector. Once the detected oxygen volume fraction drops below 0.3 %, the needle and pipe are removed, and the holes are subsequently sealed. Devices I and II are then carefully connected to form an air–SF_6 interface. The small height of the experimental channel (8 mm) ensures effective confinement of the interface by the upper and lower boundaries, thus eliminating the need for a support structure. Compared with the soap-film technique (Luo *et al.* 2016; Liang *et al.* 2019), which can also produce initial interfaces without diffusion layer and support structure, the polyester-film technique possesses an additional advantage: a significantly longer maintainable duration. This advantage is particularly crucial for the present experiments, as the interval from gas filling to shock initiation is considerably longer than that in the weak-shock experiments.

Five distinct interface configurations, including the single-mode, circular-arc, V-shaped, trapezoidal and square-waveform geometries, are considered, with the corresponding profiles illustrated in figure 3. The perturbation wavelength (λ) is fixed at 40 mm, and

https://doi.org/10.1017/jfm.2026.11512 Published online by Cambridge University Press

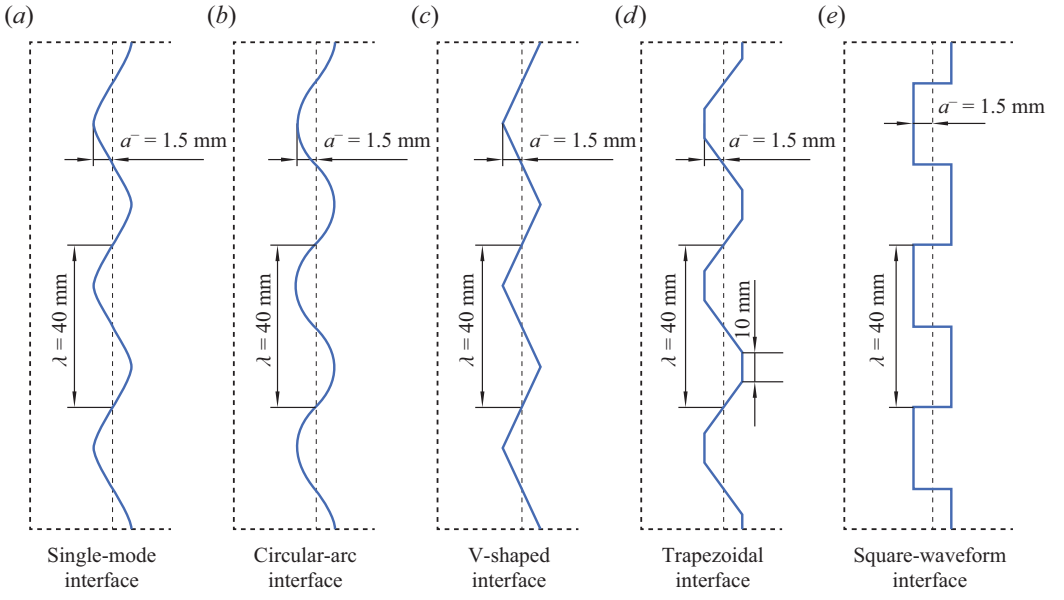


Figure 3. Schematics of initial interface configurations, where a^- is initial amplitude, and λ is perturbation wavelength.

the scaled initial amplitude (ka^-, where k and a^- denote the perturbation wavenumber and initial amplitude, respectively) is set to 0.236 to minimise the potential influence of high initial amplitude on perturbation evolution. The trapezoidal interface is assigned base length 10 mm, representing a transitional form between the V-shaped and square-waveform interfaces, which can be considered as trapezoids with base lengths 0 and 20 mm, respectively. To quantify the differences in initial modal composition, the interface profiles are expanded in a Fourier series as $y = a^- \sum_i c_i \cos(ikx)$, with the corresponding coefficients c_i ($i = 1, 2, 3, \ldots$) summarised in table 1. Notably, only the coefficients of the odd-order modes are listed, since those of the even-order modes vanish identically. For the circular-arc interface, c_1 is close to unity, and the absolute values of the coefficients for higher-order modes are small, suggesting that it deviates slightly from the single-mode interface. For the V-shaped interface, all coefficients share the same sign, with c_1 substantially smaller than unity. For the trapezoidal (square-waveform) interface, c_1 is slightly (significantly) greater than unity, and the absolute values of the coefficients for higher-order modes are relatively small (large). From the modal perspective, the circular-arc interface exhibits the smallest deviation from the single-mode configuration, whereas the square-waveform interface exhibits the largest deviation. By contrast, for the V-shaped and trapezoidal interfaces, the modal amplitudes do not provide a consistent indication of which interface deviates more markedly from the single-mode configuration. Notably, to assess the repeatability of the experiments, two separate runs have been conducted for each interface configuration. As shown in Appendix A, the key parameters of the repeated runs are in close agreement, confirming the repeatability of the experiments. For clarity, only the first run for each interface configuration is considered in the following discussion, and each case is designated according to the interface morphology.

The flow field is illuminated using a light source (CEL-PF300-T10) and captured by a high-speed video camera (Phantom V2012) through a shadowgraph imaging system, as shown in figure 2(*b*). The camera operates at 100 000 frames per second

https://doi.org/10.1017/jfm.2026.11512 Published online by Cambridge University Press

Interface configuration	c_1	c_3	c_5	c_7	$\cdots$
Single-mode	1.000	0.000	0.000	0.000	$\cdots$
Circular-arc	1.034	−0.044	0.008	−0.004	$\cdots$
V-shaped	0.811	0.090	0.032	0.016	$\cdots$
Trapezoidal	1.108	−0.076	−0.055	0.003	$\cdots$
Square-waveform	1.257	−0.396	0.211	−0.124	$\cdots$

Table 1. Coefficients of initial modal components for single-mode and quasi-single-mode interfaces.

Case	MF	A	T	M_s	v_t	Δu	$\dot{a}_l^e$	$\dot{a}_l^{imp}$
Single-mode	99.37 %	0.80	296.6	3.16 ± 0.1	610.8	552.1	30.3 ± 0.9	51.5
Circular-arc	99.63 %	0.80	296.6	3.17 ± 0.1	612.2	554.3	25.7 ± 0.9	51.7
V-shaped	99.58 %	0.80	294.0	3.17 ± 0.1	614.3	554.3	34.6 ± 1.1	51.4
Trapezoidal	99.64 %	0.80	294.3	3.22 ± 0.1	621.8	565.3	28.6 ± 1.3	52.3
Square-waveform	98.92 %	0.80	296.3	3.13 ± 0.1	604.3	545.5	28.4 ± 1.5	50.9

Table 2. Significant parameters for five experiments with various initial interface configurations: MF is the mass fraction of SF_6 downstream of the initial interface; $A = (\rho_2 - \rho_1)/(\rho_2 + \rho_1)$ is the post-shock Atwood number, with ρ_1 and ρ_2 denoting the densities of gases upstream and downstream of the post-shock interface, respectively; T is the ambient temperature; M_s is the Mach number of the incident shock; v_t is the velocity of the transmitted shock; Δu is the interface velocity jump; $\dot{a}_l^e$ and $\dot{a}_l^{imp}$ are the linear amplitude growth rates obtained from experiments and predicted by the impulsive model, respectively. Units of parameters representing velocity (or amplitude growth rate) and temperature are m s^{-1} and K, respectively.

with exposure time 1 µs, yielding spatial resolution approximately 0.57 mm per pixel. The ambient pressure and temperature are 101.3 ± 0.8 kPa and 295.3 ± 1.3 K, respectively. The gas upstream of the interface is considered to be pure air owing to the favourable sealing property of the polyester film, and the downstream gas component is determined by matching the velocity of the transmitted shock measured experimentally with that predicted using the one-dimensional gas dynamics theory. Key experimental parameters for the five experiments, including the mass fraction of SF_6 downstream of the initial interface (MF), post-shock Atwood number (A), velocity of the transmitted shock (v_t) and interface jump velocity (Δu), are summarised in table 2. The close agreement of these parameters across different experiments further demonstrates the high experimental reproducibility. Moreover, to assess the reliability of the experimental measurements, Appendix A presents a discussion of the measurement uncertainties in interface amplitude, linear amplitude growth rate, and M_s. These analyses, together with the quantitative results presented in table 2 and figures 6–10, confirm the reliability of the experimental measurements.

3. Flow features under strong-shock conditions

The experimental shadowgraph images of the evolution of single-mode and quasi-single-mode interfaces accelerated by a strong shock wave are presented in figure 4. The temporal origin ($t = 0$ µs) is defined as the moment when the incident shock reaches the mean position of the initial interface. For clarity, the shadows caused by the device edges, which convey no flow information, are removed from the images through post-processing after the shocks and interface have separated from them. It is noteworthy that

https://doi.org/10.1017/jfm.2026.11512 Published online by Cambridge University Press

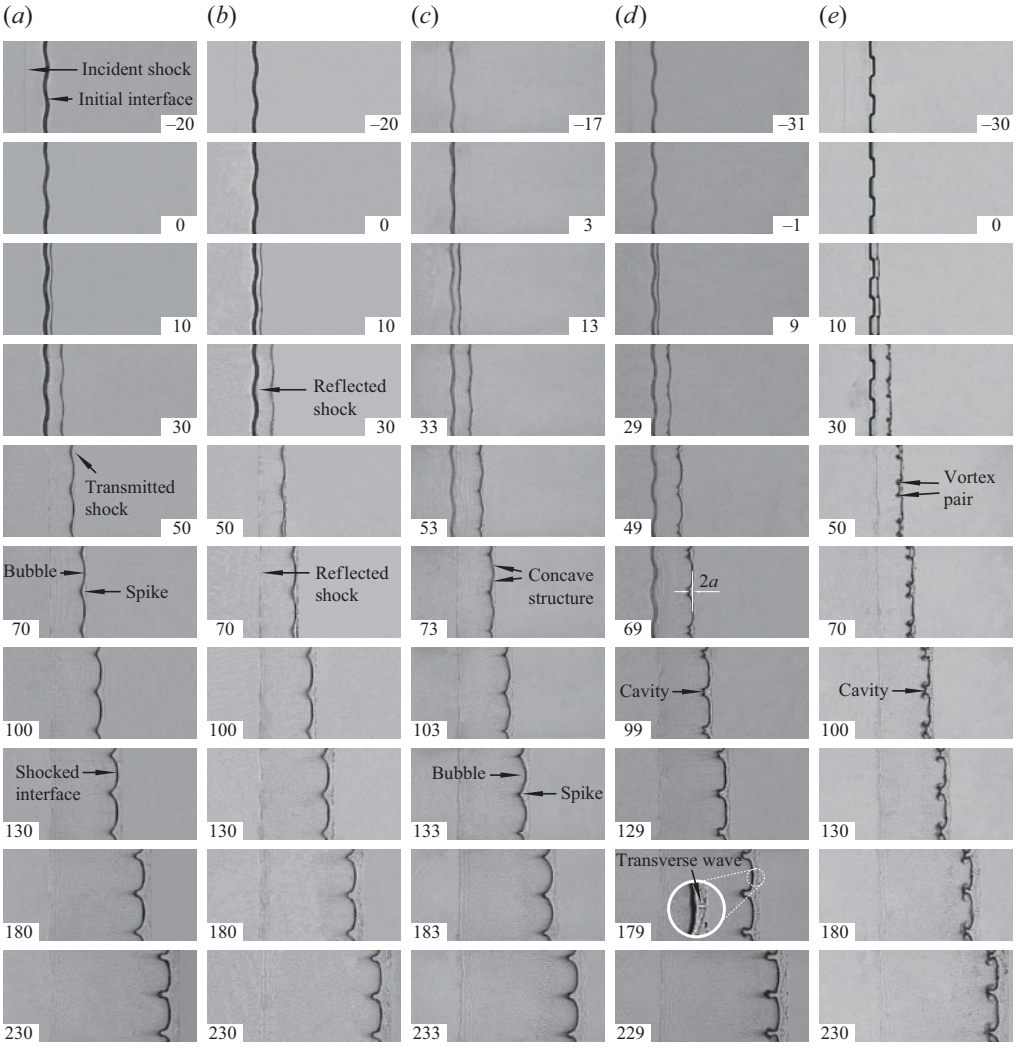


Figure 4. Experimental shadowgraphs of the evolution of single-mode and quasi-single-mode interfaces accelerated by strong shock waves: (*a*) single-mode interface; (*b*) circular-arc interface; (*c*) V-shaped interface; (*d*) trapezoidal interface; (*e*) square-waveform interface. Here, a is interface amplitude, and numbers represent the time in μs.

the observed physical areas are slightly different from run to run, which constitutes the primary reason why the interface displacement trends among different cases in figure 4 are not completely consistent with the quantitative Δu values listed in table 2. Owing to the high shock intensity involved in the present experiments, mechanical vibrations generated during shock propagation through the shock tube can induce slight shifts in the shadowgraph optical path from run to run. Nevertheless, this does not compromise the quantitative analysis, because all parameters for each individual run are extracted based on its corresponding observed area. Specifically, the spatial calibration for each run is performed independently using an identical optical set-up and the same calibration procedure, thereby ensuring that the measured data remain directly comparable across different cases.

https://doi.org/10.1017/jfm.2026.11512 Published online by Cambridge University Press

In the single-mode case, which serves as a reference for the quasi-single-mode scenarios, the reflected and transmitted shocks are generated when the incident shock impacts the initial interface. The reflected shock propagates downstream because the Mach number of the flow ahead (up to 1.4) exceeds its own Mach number (1.3). This behaviour is consistent with the theoretical analysis of Mikaelian (2016), which demonstrates that the reflected shock propagates downstream for flows initiated by an incident shock with $M_s > 2.76$, and upstream for that with $M_s < 2.76$, with $M_s = 2.76$ corresponding to the special case of a standing shock at rest. At early times ($t < 10\,\mu$s), the reflected shock overlaps the shadows from the device edges, while the transmitted shock remains close to the shocked interface, making them indistinguishable. Notably, the relative separation velocity of the transmitted shock from the shocked interface, defined as $(v_t - \Delta u)/v_t$, in the present experiments (~ 0.095) is significantly lower than that under weak-shock conditions reported by Liang *et al.* (2019) (~ 0.62). Shortly after these discontinuities become distinguishable, distinct spike and bubble structures emerge ($t = 70\,\mu$s). Owing to the compressibility effects introduced by the strong shock wave (Si *et al.* 2025), the bubble front remains significantly flatter than that under weak-shock conditions (Li *et al.* 2023) throughout the evolution process.

The circular-arc interface exhibits evolution closely resembling that of the single-mode interface, due to only slight differences in modal composition. In contrast, other quasi-single-mode interfaces exhibit significant morphological deviations relative to the single-mode interface. For the V-shaped case, during the early stage ($t < 103\,\mu$s), the tips of the bubble and spike are sharper than in the single-mode case, accompanied by the emergence of small concave structures in between. Subsequently, these concave structures vanish gradually and the bubble flattens. The spike remains sharp until the intermediate stage (133 μs), yet ultimately evolves towards the late-stage morphology of the single-mode interface (233 μs).

For the trapezoidal and square-waveform cases, a cavity emerges at the spike tip in the early period. This phenomenon results from a vortex pair arising from strong vorticity deposited at the upstream corners during shock impact, which initially rolls up upstream, as illustrated in figure 5(*a*). In particular, in the square-waveform case, where the upstream corners are sharper than those in the trapezoidal case, a pronounced vortex pair and cavity form at a very early stage (10–30 μs). As the interface evolves, the cavity progressively vanishes under the action of the vortex-pair-induced velocity field, which directs upstream at the spike tip, as sketched in figure 5(*b*). At the upper (lower) junction of the spike and bubble, the perturbed velocity field directs upwards (downwards), thereby driving the expansion of the bubble front and narrowing of the spike stem. In the square-waveform case, the strong vortex pair drives the portion of the interface between the bubble tip and spike–bubble junction downstream more rapidly than the bubble tip itself, producing a concave bubble tip throughout the evolution. In contrast, the comparatively weaker vortex pair in the trapezoidal case induces only a slight concavity at the bubble tip during the intermediate stage ($\sim 69-129\,\mu$s).

4. Amplitude evolution in highly compressible flow

In this study, following the convention in RMI studies (Zhou *et al.* 2021; Zhou 2024), the overall interface amplitude (a) is defined as $(|a_b| + |a_s|)/2$, where a_b and a_s denote the bubble and spike amplitudes, respectively. Specifically, a_b (a_s) is defined as the streamwise coordinate difference between the bubble (spike) tip and the mean interface position. At the early time, the experimental $a_{b/s}$ and the interface velocity jump Δu are determined according to the mean positions of the shocked interface obtained via Fourier

https://doi.org/10.1017/jfm.2026.11512 Published online by Cambridge University Press

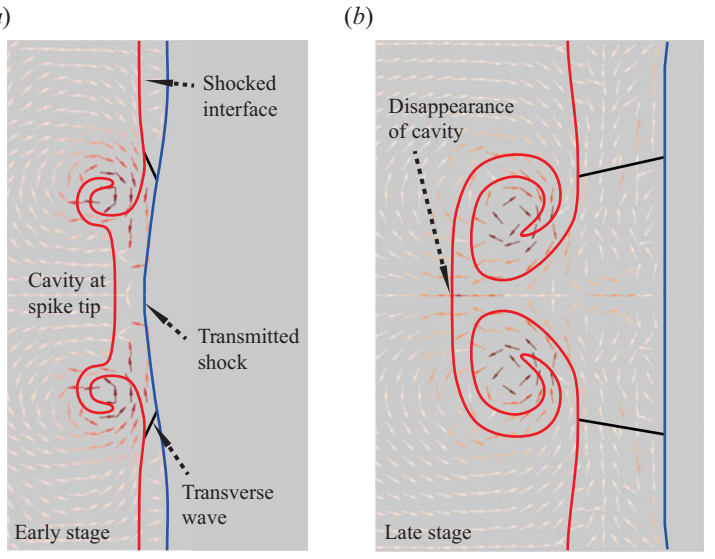


Figure 5. Sketches of the shock waves and interface morphology at the early and late stages for trapezoidal and square-waveform cases, along with the perturbed velocity field in the region behind the transmitted shock, obtained by subtracting the background one-dimensional velocity in the area between transmitted and reflected shocks from the particle velocity field. The colour of the arrow represents the magnitude of the velocity: the darker the colour, the greater the velocity. Red, blue and black lines denote the shocked interface, transmitted shock and transverse wave, respectively.

analysis. A detailed description of the Fourier-based data processing procedure can be found in Appendix B. At later stages, however, when vortex roll-up becomes significant, the interface can no longer be accurately described as a single-valued function. Under such conditions, the Fourier-based method is no longer reliable and may introduce significant errors. Consequently, the mean interface position is no longer directly determined from the interface contour. Instead, it is obtained by extrapolating the mean interface positions determined at the earlier time based on Δu, thereby enabling the determination of a_b and a_s throughout the entire interface evolution.

The amplitude evolution typically proceeds through three successive stages: start-up, linear and nonlinear (Zhou 2024). In the start-up stage (Lombardini & Pullin 2009), the amplitude growth rate ($\dot{a}$) rises from zero and gradually reaches an asymptotic value ($\dot{a}_l$) under the drive of pressure perturbations. Afterwards, $\dot{a}$ remains approximately constant over a period known as the linear stage. As the flow evolves further and nonlinearity becomes pronounced, $\dot{a}$ decreases, marking the onset of the nonlinear evolution stage.

4.1. *Start-up to linear evolution stages*

The amplitude evolution of different interfaces from the start-up stage to the linear stage is presented in figure 6 in dimensionless form. Here, t and a are normalised to $\tau = k\dot{a}_l^e t$ and $\alpha = ka$, respectively, where $\dot{a}_l^e$ represents the experimental $\dot{a}_l$. For the single-mode, circular-arc, trapezoidal and square-waveform cases, $\dot{a}$ increases until $\tau \approx 0.38$, after which it remains nearly constant until $\tau \approx 0.57$. In contrast, $\dot{a}$ for the V-shaped interface rapidly reaches its peak value, after which it remains nearly constant until $\tau \approx 0.49$. The earlier onset of the nonlinear regime for the V-shaped interface is attributed to its modal composition. The V-shaped interface contains exclusively positive higher-order Fourier modes, thereby leading to a more rapid evolution at the early time compared with the

https://doi.org/10.1017/jfm.2026.11512 Published online by Cambridge University Press

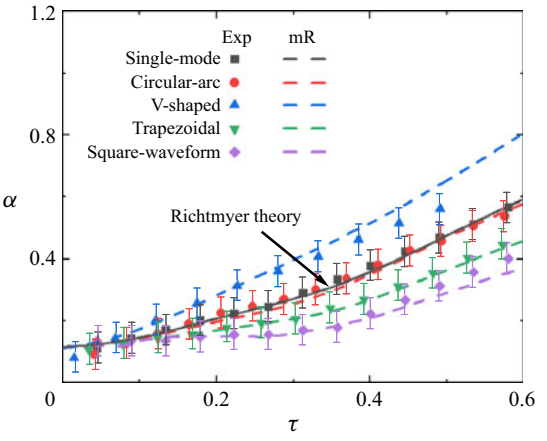


Figure 6. Dimensionless amplitude evolution of single-mode and quasi-single-mode interfaces from the start-up to linear stages. Symbols indicate experimental data; solid and dashed lines indicate predictions from Richtmyer theory and the mR model, respectively, where the mR model denotes the model obtained by extending the Richtmyer theory through linear superposition. Note that the predictions of the Richtmyer theory and mR model coincide for the single-mode case.

single-mode interface and other quasi-single-mode interfaces containing both positive and negative modes (Liang *et al.* 2019; Guo *et al.* 2022). As a result, the linear regime of the V-shaped interface ends earlier.

The classical linear model proposed by Richtmyer (1960) (impulsive model), which has been validated for weak-shock-driven single-mode RMI (Chen *et al.* 2023), is first considered as a theoretical reference for comparison with the experiments. The model can be expressed as

$$\dot{a}_l^{imp} = k\,\Delta u\,Aa^{+}. \tag{4.1}$$

Here, $a^{+} = a^{-}(1 - \Delta u/v_{is})$ represents the post-shock amplitude, where v_{is} denotes the incident shock velocity. It is worth noting that for the quasi-single-mode interfaces, the amplitude adopted for prediction is also the overall initial interface amplitude a^{-}, i.e. the amplitude resulting from the superposition of all Fourier modes, rather than the amplitude of the fundamental Fourier component alone. This choice is made for comparative purposes, allowing the influence of higher-order modes to be evaluated indirectly by comparing $\dot{a}_l^{e}$ and $\dot{a}_l^{imp}$ across different interface configurations (Liang *et al.* 2019). Moreover, the minor differences in $\dot{a}_l^{imp}$ reported in table 2 are due to slight variations in the initial flow conditions rather than differences in the computational procedure. The comparison between $\dot{a}_l^{e}$ and $\dot{a}_l^{imp}$ indicates that higher-order modes influence the linear evolution, and the impulsive model fails to accurately predict $\dot{a}_l^{e}$ even for the single-mode case. This failure stems from the inadequacy of the model's empirical correction – i.e. using a^{+} and A instead of the pre-shock counterparts for prediction – in capturing the influence of compressibility on interface evolution in highly compressible flow (Mikaelian 1994; Yang, Zhang & Sharp 1994; Wouchuk 2001; Napieralski *et al.* 2024; Si *et al.* 2025).

In addition to the impulsive model, Richtmyer (1960) also proposed a compressible linear theory (Richtmyer theory) that is theoretically valid for strongly compressible flows. As shown in figure 6, the Richtmyer theory effectively captures the early-time amplitude evolution of the single-mode RMI. Notably, although previous work (Si *et al.* 2025) experimentally verified its capability to predict $\dot{a}_l$ under highly compressible conditions,

https://doi.org/10.1017/jfm.2026.11512 Published online by Cambridge University Press

the present study provides the first experimental evidence supporting its applicability in describing the strong-shock-driven single-mode RMI evolution from the start-up to linear stages. In contrast, this theory underestimates the early-time evolution of the V-shaped interface, and overestimates the growth of the circular-arc, trapezoidal and square-waveform interfaces. This highlights that higher-order modes play a significant role in the early-time evolution of quasi-single-mode interfaces, and must be taken into account.

Assuming that the amplitude evolution of a quasi-single-mode interface is the linear superposition of the growth of each initial mode (Mikaelian 2005), and that the contribution of harmonic modes (i.e. modal components arising from coupling) is negligible, a linear model for quasi-single-mode RMI (referred to as the mR model) is constructed as follows:

$$\begin{aligned} \dot{a}^{mR}(t) &= \sum_i c_i\, \dot{a}_i^R(t), \quad i = 1, 2, 3, \ldots, \\ a^{mR} &= \int \dot{a}^{mR}\, \mathrm{d}t = \int \sum_i c_i \dot{a}_i^R\, \mathrm{d}t \\ &= \sum_i c_i\, a_i^R(t), \quad i = 1, 2, 3, \ldots. \end{aligned} \tag{4.2}$$

Here, $\dot{a}_i^R$ and a_i^R represent the amplitude growth rate and amplitude predicted by the Richtmyer theory for the ith-order initial mode with initial amplitude a^-, respectively. The predictions of the mR model for all cases are plotted in figure 6. It is noteworthy that the predictions of the mR model and the Richtmyer theory for the single-mode case are identical. The mR model provides a reasonable prediction of the experimental amplitude evolution from the start-up to the linear stages across all cases. These results indicate the validity of the assumptions underlying the mR model, i.e. the early-time evolution of quasi-single-mode RMI can be regarded as the linear superposition of the growth of each initial mode, with modal coupling remaining negligible.

4.2. *Nonlinear evolution period*

The temporal evolutions of a and $a_{b/s}$ are presented in figures 7(a) and 7(b), respectively, in dimensionless form. Here, t, a and $a_{b/s}$ are normalised as $\tau = k\dot{a}_l^e(t - t^m)$, $\alpha = k(a - a^m)$ and $\alpha_{b/s} = k(a_{b/s} - a_{b/s}^m)$, respectively, where t^m represents the moment when $\dot{a}$ reaches $\dot{a}_l^e$, and a^m ($a_{b/s}^m$) corresponds to the value of a ($a_{b/s}$) at $t = t^m$. It is observed that the overall amplitude evolutions for the five experimental cases nearly collapse together, showing partial discrepancy with the findings of Liang *et al.* (2019): the dimensionless amplitude growths of the single-mode, circular-arc, trapezoidal and square-waveform interfaces are similar, yet lower than that of the V-shaped interface. This discrepancy can be attributed to the pronounced compressibility effects, including the shock-proximity effect (Rikanati *et al.* 2003) and the associated influence of transverse waves, propagating in the region between the transmitted shock and shocked interface, on interface evolution (i.e. the secondary-compression effect) (Si *et al.* 2025). Notably, these effects are more pronounced when the interface is located closer to the transmitted shock. As illustrated in figure 6, the V-shaped interface evolves considerably faster than the others in the early periods, bringing the bubble closer to the transmitted shock. As a result, the V-shaped interface experiences stronger compressibility-induced suppression on the evolution at later times, offsetting its initially faster growth, and yielding a final amplitude comparable to amplitudes of the others.

https://doi.org/10.1017/jfm.2026.11512 Published online by Cambridge University Press

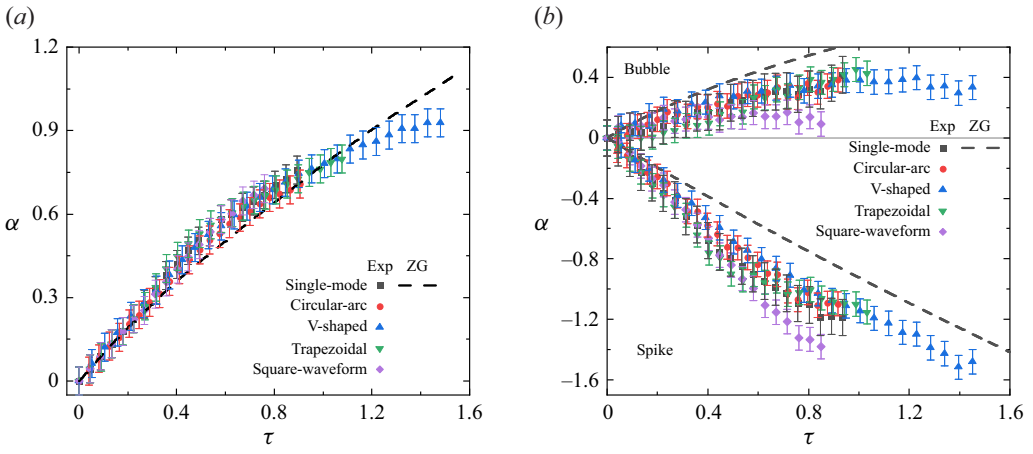


Figure 7. Temporal amplitude variations obtained from experiments (symbols) and predicted by the ZG model (dashed lines): (*a*) overall interface; (*b*) bubble and spike.

Concerning the amplitude growth of the bubble and spike, the square-waveform interface exhibits certain differences in evolution rate relative to the other interface configurations. Its slow bubble development arises from the initially flat front, whereas its rapid spike evolution is driven by the strong vortex pair, which promotes the upward motion of the spike tip. The other quasi-single-mode interfaces also exhibit distinct bubble and spike evolution rates relative to the single-mode interface. However, as their modal compositions are closer to the single-mode case compared with the square-waveform interface, the resulting differences in amplitude evolution are relatively minor. The nonlinear model proposed by Zhang & Guo (2016) (the ZG model), which has been validated for weak-shock-driven RMI at a single-mode air–SF_6 interface (Chen *et al.* 2023), is considered here as a theoretical reference. The ZG model can be expressed as

$$\dot{a}_{b/s}^{ZG} = \frac{\dot{a}_l^e}{1 + \xi_{b/s} k \dot{a}_l^e t}, \tag{4.3}$$

where

$$\xi_{b/s} = \frac{3}{4} \frac{(1 \pm |A|)(3 \pm |A|)}{3 \pm |A| + \sqrt{2(1 \pm |A|)}} \frac{4(3 \pm |A|) + \sqrt{2}(9 \pm |A|)(1 \pm |A|)^{1/2}}{(3 \pm |A|)^2 + 2\sqrt{2}(3 \mp |A|)(1 \pm |A|)^{1/2}}, \tag{4.4}$$

with the $+$ and $-$ signs referring to the bubble and spike, respectively. For the present experiments with $A = 0.8$, we have $\xi_b = 1.34$ and $\xi_s = 0.17$. The predictions of the ZG model are presented in figure 7 for comparison. The model appears to reproduce the overall amplitude growth reasonably well, which, however, is a coincidence arising from the simultaneous overestimation of the bubble growth and underestimation of the spike evolution. Moreover, its predictive performance for the square-waveform case is particularly poor.

The failure of the ZG model in describing the present strong-shock experiments can be traced to three physical mechanisms that exert significant influences yet were not incorporated. First, compressibility effects, including the shock proximity and secondary compression: for the shock-proximity effect, the transmitted shock travels at a velocity comparable to the interface and stays near it for a prolonged period under strong-shock conditions, which was first pointed out by Mikaelian (1994) and also discussed in Mikaelian (2016). The interface is unable to penetrate the shock front, thus the

https://doi.org/10.1017/jfm.2026.11512 Published online by Cambridge University Press

evolution of the downstream interface structure (i.e. bubble for the light–heavy interface considered here) is significantly suppressed (Rikanati *et al.* 2003; Sadot *et al.* 2003). For the secondary-compression effect, the interaction between the incident shock and the disturbed interface produces a perturbed transmitted shock that subsequently develops into a Mach reflection with accompanying transverse waves. These transverse waves introduce pressure fluctuations in the vicinity of the interface, which further affect the interface evolution (Sadot *et al.* 2003; Guo *et al.* 2020). Second, the spike-acceleration effect: at high A, higher-order harmonic modes progressively concentrate at the spike tip and promote the spike growth (Dimonte & Ramaprabhu 2010; Chen *et al.* 2023; Si *et al.* 2025). Third, the higher-order-mode effect arises from the presence of additional initial modes. The ZG model was originally developed for single-mode RMI, and the higher-order initial modes, which are intrinsic to quasi-single-mode RMI and affect both the bubble and spike evolution (Liang *et al.* 2019), were not considered.

The preceding analysis indicates that an effective model for describing the evolution of strong-shock-driven quasi-single-mode RMI must incorporate the coupled influences of the higher-order modes, shock proximity, secondary compression and spike acceleration. Developing such a model from first principles is highly challenging. Here, we propose an empirical extension of the ZG model, referred to as the ε-ZG model, which is formulated as

$$\dot{a}_b^{\varepsilon ZG} = \frac{\dot{a}_l^e}{1 + \xi_b^{\varepsilon ZG} k \dot{a}_l^e t}, \tag{4.5}$$

$$\dot{a}_s^{\varepsilon ZG} = \frac{H_s \dot{a}_l^e}{1 + \xi_s k \dot{a}_l^e t + H_s (k \dot{a}_l^e t)^2}, \tag{4.6}$$

in which

$$\begin{aligned} \xi_b^{\varepsilon ZG} &= F_b \xi_b + G_b, \\ F_b(\varepsilon) &= 1 - 20\varepsilon, \\ G_b(\varepsilon, M_s) &= 1.5(\varepsilon + 1)(M_s - 1)\, \mathrm{e}^{-5k\dot{a}_l^e t}, \\ H_s(\varepsilon, A) &= 1 + A - \varepsilon, \\ \varepsilon &= \frac{c_3}{c_1 + c_3}. \end{aligned} \tag{4.7}$$

The ε-ZG model is formulated by incorporating the effects of the higher-order modes, shock proximity, secondary compression and spike acceleration into the framework of the ZG model in an empirical yet physically guided manner. For the higher-order-mode effect, which influences both the bubble and spike evolution, a coefficient ε – i.e. the ratio of the third-order modal coefficient to the sum of the first- and third-order modal coefficients – is introduced to provide a simplified characterisation: Fourier analysis shows that the coefficients of the first- and third-order modes constitute the majority of the total modal amplitude, while those of higher-order modes contribute only marginally. For the bubble evolution, two dominant physical mechanisms are identified based on the present experiments: first, the higher-order-mode effect, which acts continuously throughout the evolution; second, compressibility effects, including shock proximity and secondary compression. These two effects are incorporated into the modified framework through the term $\xi_b^{\varepsilon ZG} = F_b \xi_b + G_b$. The factor F_b, including ε, represents the continuous influence of the higher-order-mode effect, while G_b primarily accounts for the suppression arising from compressibility effects. We formulate G_b as a time-decaying function to

https://doi.org/10.1017/jfm.2026.11512 Published online by Cambridge University Press

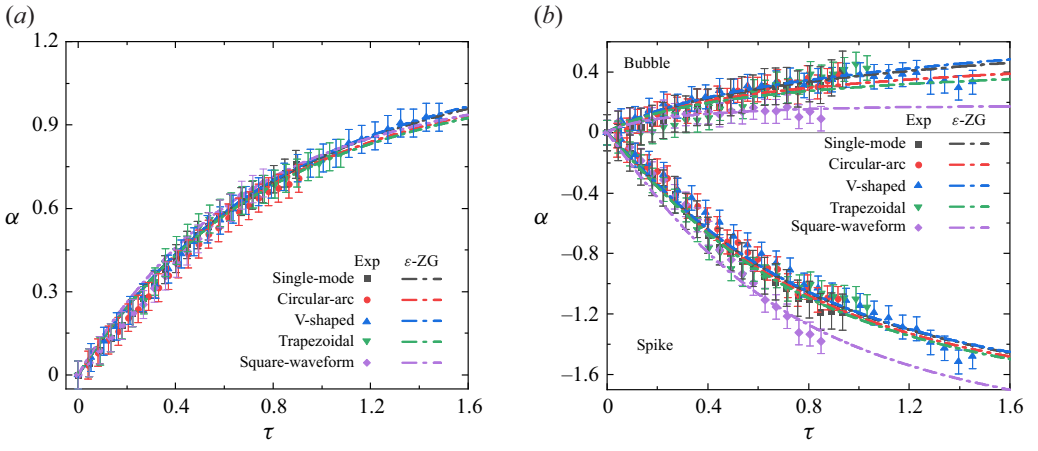


Figure 8. Temporal amplitude variations obtained from experiments (symbols) and predicted by the ε-ZG model (dash-dotted line): (*a*) overall interface; (*b*) bubble and spike.

represent the gradual attenuation of compressibility effects as the transmitted shock separates from the interface. For the spike evolution, two dominant physical effects are similarly identified based on the present experiments: first, the higher-order-mode effect acting continuously throughout the evolution; second, the spike-acceleration effect, which is associated with the progressive accumulation of harmonic modes near the spike tip during evolution. These two effects are incorporated into the modified framework through the coefficient H_s, which incorporates both ε, characterising the higher-order-mode effect, and A, representing the spike-acceleration effect. Here, H_s appears in both $H_s\dot{a}_l^e$ and $H_s(k\dot{a}_l^e t)^2$: $H_s\dot{a}_l^e$ represents the influence of the two effects on the initial spike growth, while $H_s(k\dot{a}_l^e t)^2$ accounts for their continued contributions during subsequent spike evolution.

The predictions of the ε-ZG model are presented in figure 8, demonstrating that it successfully captures the amplitude evolution of the overall interface, bubble and spike across all cases.

4.3. *Complete amplitude evolution from start-up to nonlinear phases*

In the quantitative analysis presented above, two new models, i.e. the mR and ε-ZG models, have been developed to describe the amplitude evolution during the start-up-to-linear and nonlinear stages, respectively. Although each model reasonably captures the RMI evolution in the corresponding period, a theoretical framework that describes the complete amplitude evolution from the early start-up to the late nonlinear stage is more desirable. To achieve this, we employ a matching strategy to bridge the linear and nonlinear models describing the interface evolution. However, a key issue concerns where these two models should be connected, i.e. when the perturbation evolution can be considered to transition from the linear regime to the nonlinear regime. In the start-up period, $\dot{a}$ gradually approaches $\dot{a}_l^e$, while nonlinearity may already emerge at this early stage. However, provided that ka^- is small, the influence of nonlinearity on amplitude evolution could remain limited during the start-up period and for some time thereafter. Within this subsequent period, the amplitude evolution can still be approximated as linear, thus it is referred to as the linear stage (Wouchuk 2001). When nonlinearity becomes apparent and $\dot{a}$ falls below $\dot{a}_l^e$, the amplitude evolution is considered to enter the nonlinear stage (Dimonte & Ramaprabhu 2010; Zhang & Guo 2016). Notably, the linear stage is an

https://doi.org/10.1017/jfm.2026.11512 Published online by Cambridge University Press

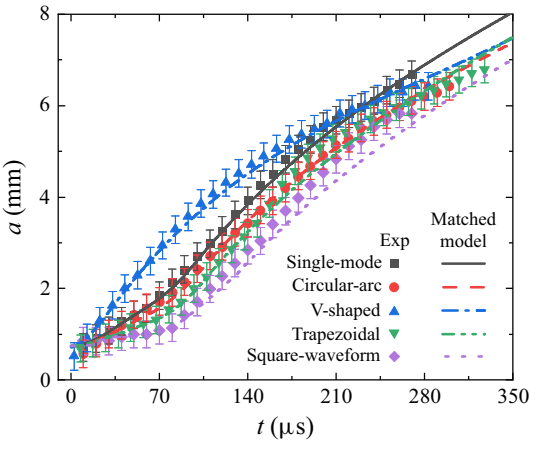


Figure 9. Comparison of the experimental measurements and matched model predictions for the complete amplitude evolution from the early-time start-up to the late-time nonlinear stage.

approximate description of a period where nonlinearity may exist but remains limited, i.e. linear amplitude evolution does not necessarily imply a strictly linear physical process. Consequently, it is challenging to rigorously define the demarcation point of the so-called linear stage from the nonlinear stage. In the present work, the end of the start-up period, i.e. the moment at which $\dot{a}$ first reaches $\dot{a}_l^e$ (t^m), is taken as the transition point separating the linear and nonlinear physical processes, as well as the boundary between the regimes represented by the mR and ε-ZG models. The matched model is formulated as

$$\dot{a}^{match}(t) = \begin{cases} \dot{a}^{mR}(t), & t \leqslant t^m, \\ \dot{a}^{\varepsilon ZG}(t - t^m), & t > t^m. \end{cases} \tag{4.8}$$

Here, $a^{match}(0) = a^+$ and $\dot{a}^{\varepsilon ZG}(t) = [\dot{a}_b^{\varepsilon ZG}(t) + \dot{a}_s^{\varepsilon ZG}(t)]/2$. The complete amplitude evolution can then be obtained by integrating $\dot{a}^{match}(t)$ over time. It should be emphasised that the matched model does not imply an abrupt physical transition, but instead establishes a continuous connection between the linear solution and the nonlinear evolution law.

The predictions of the matched model are presented in figure 9 alongside the experimental data for comparison. The results demonstrate that the model provides a reasonable prediction for the complete amplitude evolution of all five experiments. To further evaluate the matched model, the experimentally measured and theoretically predicted dimensional evolutions of a_b and a_s are presented in figures 10(a) and 10(b), respectively. The matched model reasonably predicts the bubble and spike amplitude evolutions individually. This indicates that the favourable agreement observed in figure 9 does not arise from compensating errors but instead reflects the model's capability to describe both components separately.

The above comparison indicates that although the interface evolution under strong-shock conditions differs from the weak-shock scenario, where the amplitude growth can be simply divided into a linear compressible stage followed by a nonlinear incompressible stage (Zhang & Sohn 1997), the idea of modelling the complete amplitude evolution through matching the linear and nonlinear solutions remains applicable. This offers some insights for the future development of models for strong-shock-driven RMI.

https://doi.org/10.1017/jfm.2026.11512 Published online by Cambridge University Press

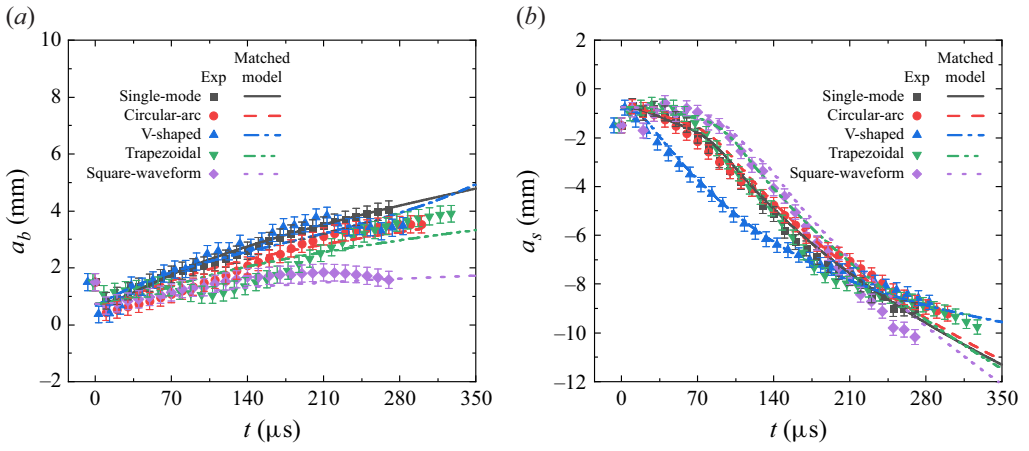


Figure 10. Comparison of the experimental measurements and matched model predictions for the amplitude evolution of (*a*) the bubble and (*b*) the spike from the early-time start-up to the late-time nonlinear stage.

4.4. *Comparison between quasi-single-mode RMI in weak- and strong-shock regimes*

To elucidate the differences in the evolution mechanisms between quasi-single-mode RMI under weak- and strong-shock conditions, it is instructive to compare the present findings with those reported in previous studies on weak-shock-induced quasi-single-mode RMI (Bakhrakh *et al.* 1995; Liang *et al.* 2019; Guo *et al.* 2022). Notably, the interface configurations considered by Liang *et al.* (2019) and in the present study are identical. Accordingly, the results of Liang *et al.* (2019) are regarded as representative of quasi-single-mode RMI under weak-shock conditions, and are used for direct comparison with the present results.

Regarding the linear stage, Liang *et al.* (2019) reported that the impulsive model accurately describes single-mode RMI under weak-shock conditions. For quasi-single-mode interfaces, $\dot{a}_l^e$ deviates from $\dot{a}_l^{imp}$ as the interface deviates from a single-mode configuration, indicating that higher-order initial modes significantly affect the linear evolution (Liang *et al.* 2019). In the present strong-shock experiments, the impulsive model cannot describe the early-time dynamics of the single-mode interface well, because it fails to adequately account for flow compressibility (Mikaelian 1994; Yang *et al.* 1994; Wouchuk 2001; Napieralski *et al.* 2024; Si *et al.* 2025). In contrast, the compressible linear theory provides an accurate description of the single-mode case. For quasi-single-mode interfaces, higher-order initial modes likewise influence the early-time evolution, and their effects can be incorporated via linear superposition within the framework of the compressible linear theory.

Regarding the nonlinear stage, Liang *et al.* (2019) reported that weak-shock-induced single-mode RMI can be accurately described by the ZG model, while the quasi-single-mode cases can be described by extending the ZG model through linear superposition of the contributions from individual modes. The validity of this superposition-based approach suggests that modal coupling remains weak, and that the nonlinear quasi-single-mode interface evolution is governed by the intrinsic nonlinearity captured by the ZG model, together with contributions from higher-order initial modes. Under strong-shock conditions, modal coupling also remains weak. However, in addition to intrinsic nonlinearity and the influence of higher-order initial modes, compressibility effects, including shock proximity and secondary compression, additionally affect the evolution law.

https://doi.org/10.1017/jfm.2026.11512 Published online by Cambridge University Press

In summary, higher-order modes influence the linear and nonlinear evolution under both weak- and strong-shock conditions. The primary distinction between the two regimes lies in the degree of the compressibility, which leads to differences in the evolution characteristics and in the predictive performance of the corresponding models.

5. Conclusions

This study experimentally investigates the strong-shock-driven Richtmyer–Meshkov instability (RMI) at quasi-single-mode interfaces employing a novel shock-tube facility combined with an advanced interface-generation technique, with the incident shock Mach number reaching 3.18 ± 0.05. One canonical single-mode and four quasi-single-mode configurations, including the circular-arc, V-shaped, trapezoidal and square-waveform geometries, are considered to evaluate the influence of higher-order initial modes on instability evolution under strong-shock conditions.

Among the quasi-single-mode interfaces, the circular-arc interface exhibits only minor deviations in morphological evolution from the single-mode case, because they share nearly identical modal compositions. In contrast, the V-shaped, trapezoidal and square-waveform interfaces manifest markedly different evolution features. Specifically, the V-shaped interface preserves a sharp spike/bubble until the intermediate stage, yet ultimately tends towards the single-mode scenario at late times. For the trapezoidal and square-waveform interfaces, intense vorticity deposited at the upstream corners initially produces a cavity at the spike tip, which subsequently dissipates under the action of the vortex-pair-induced velocity.

Quantitatively, the classical impulsive model fails to reproduce the observed linear amplitude growth for all configurations, owing to its limitation in describing the influence of strong flow compressibility on the early-time perturbation development. For the first time, the validity of the compressible linear theory (Richtmyer 1960) in describing the single-mode interface evolution from the start-up to the linear stage is experimentally confirmed. In contrast, this theory cannot accurately predict the evolution of quasi-single-mode interfaces, indicating a significant influence of higher-order initial modes on the early-time evolution. To address this issue, a linear model assuming that the quasi-single-mode interface evolution can be regarded as the linear superposition of the growth of each initial mode is proposed. The agreement between experimental data and theoretical predictions indicates that modal coupling remains negligible during the early-time regime. In the nonlinear period, the ZG model (Zhang & Guo 2016), previously validated for the weak-shock single-mode scenario, fails to reproduce the experimental amplitude evolution for any tested configuration. This deficiency is attributed to it not considering several key mechanisms, including higher-order-mode effect, secondary compression, shock proximity and spike acceleration. Building on these findings and the ZG model, we propose an empirical model that captures the observed nonlinear amplitude evolution across all considered interface geometries. Finally, to provide a theoretical description of the complete evolution of strong-shock-driven RMI from start-up to the nonlinear regime, we construct a composite model by matching the validated linear and nonlinear solutions. The favourable agreement between experimental measurements and model predictions demonstrates the viability of this simple matching approach for modelling strong-shock-driven RMI.

Furthermore, a comparison of quasi-single-mode RMI under weak- and strong-shock conditions indicates that higher-order initial modes play a significant role throughout both the linear and nonlinear stages in both regimes. The fundamental distinction lies in the enhanced compressibility effects under strong-shock conditions, such as shock proximity

https://doi.org/10.1017/jfm.2026.11512 Published online by Cambridge University Press

Interface configuration	Run	MF	A	T	M_s	v_t	Δu	$\dot{a}_l^e$
Single-mode	1	99.37 %	0.80	296.6	3.16 ± 0.1	610.8	552.1	30.3 ± 0.9
	2	98.97 %	0.80	297.7	3.09 ± 0.1	600.2	541.3	29.1 ± 1.0
Circular-arc	1	99.63 %	0.80	296.6	3.17 ± 0.1	612.2	554.3	25.7 ± 0.9
	2	99.41 %	0.80	296.6	3.11 ± 0.1	601.4	550.2	25.1 ± 1.2
V-shaped	1	99.58 %	0.80	294.0	3.17 ± 0.1	614.3	554.3	34.6 ± 1.1
	2	99.72 %	0.80	296.4	3.19 ± 0.1	611.4	552.8	35.1 ± 1.2
Trapezoidal	1	99.64 %	0.80	294.3	3.22 ± 0.1	621.8	565.3	28.6 ± 1.3
	2	98.55 %	0.80	295.8	3.07 ± 0.1	597.5	539.2	26.3 ± 1.3
Square-waveform	1	98.92 %	0.80	296.3	3.13 ± 0.1	604.3	545.5	28.4 ± 1.5
	2	98.15 %	0.80	296.7	3.13 ± 0.1	606.1	547.2	28.1 ± 1.7

Table 3. Key parameters of the repeated runs for each interface configuration: MF is the mass fraction of SF_6 downstream of the initial interface; $A = (\rho_2 - \rho_1)/(\rho_2 + \rho_1)$ is the post-shock Atwood number, with ρ_1 and ρ_2 denoting the densities of gases upstream and downstream of the post-shock interface, respectively; T is the ambient temperature; M_s is the Mach number of the incident shock; v_t is the velocity of the transmitted shock; Δu is the interface velocity jump; $\dot{a}_l^e$ is the experimental linear amplitude growth rate. Units of parameters representing velocity (or amplitude growth rate) and temperature are m s^{-1} and K, respectively.

and secondary compression, which modify the characteristics of interface evolution and thereby affect the applicability of theoretical models.

Acknowledgements. The authors sincerely appreciate the reviewers for their valuable suggestions.

Funding. This work was supported by the National Natural Science Foundation of China (grant nos 12388101, U2430202 and 12472228), the Chinese Academy of Sciences Project for Young Scientists in Basic Research (grant no. YSBR-087), the Young Elite Scientists Sponsorship Programme by CAST (grant no. 2023QNRC001) and the New Cornerstone Science Foundation through the Xplorer Prize.

Declaration of interests. The authors report no conflict of interest.

Appendix A. Experimental repeatability and measurement uncertainty

To assess the repeatability of the experiments, we have conducted two separate runs for each interface configuration under nearly identical conditions. Table 3 summarises the key experimental parameters, including the SF_6 mass fraction downstream of the interface, post-shock Atwood number, ambient temperature, incident shock Mach number, transmitted shock velocity, interface velocity jump, and experimental linear amplitude growth rate. Close agreement between repeated runs is observed for all interface configurations, confirming the repeatability of the experiments. For clarity, only the first run for each interface configuration is considered in the main text.

Regarding the uncertainty of the interface amplitude measurement, the main source stems from the indeterminate position of the interface edge in the shadowgraph images. The spatial image resolution is 0.57 mm per pixel, and the interface edge location can be determined within ± 0.5 pixel, which corresponds to measurement uncertainty approximately ± 0.29 mm. These uncertainties are reflected by the error bars in figures 6–10, which are small relative to the overall amplitude evolution and do not affect the observed evolution behaviour.

The experimental linear amplitude growth rate ($\dot{a}_l^e$) is determined by performing a linear least squares fit to the amplitude–time data during the identified linear regime.

https://doi.org/10.1017/jfm.2026.11512 Published online by Cambridge University Press

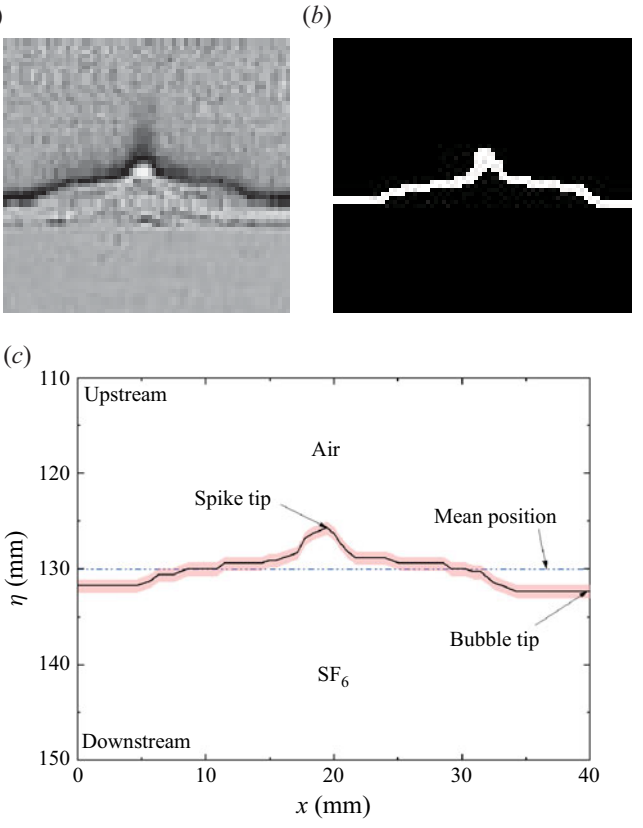


Figure 11. Image preprocessing procedures for Fourier analysis, illustrated with an example frame from the V-shaped case at $t = 103\,\mu$s: (*a*) original experimental image spanning one perturbation wavelength; (*b*) binarised image; (*c*) interface contour in physical coordinates.

Its uncertainty also primarily arises from the indeterminate position of the interface edge in the shadowgraph images, estimated as ± 0.5 pixel. To evaluate the measurement uncertainty in $\dot{a}_l^e$, the interface positions are re-measured multiple times within this range, and the largest deviation of the fitted $\dot{a}_l^e$ is taken as its uncertainty. As shown in table 2, this uncertainty is typically below 6 % of the corresponding mean value.

The shock Mach number (M_s) is determined from the shock displacement measured between consecutive shadowgraph images separated by $10\,\mu$s. The shock position uncertainty is estimated as ± 0.5 pixel, which corresponds to velocity uncertainty approximately $29\,\mathrm{m\,s^{-1}}$. This translates to an uncertainty in M_s of approximately ± 0.1, which is small relative to the corresponding central value (~ 3.18).

Appendix B. Fourier analysis and data processing

In this study, one-dimensional Fourier analysis is employed to determine the mean interface position, which serves as a reference for distinguishing the bubble and spike structures. For clarity, the Fourier analysis process is summarised in the following steps, with a frame from the V-shaped case at $t = 103\,\mu$s as a representative example.

(i) Preprocessing. A region spanning one perturbation wavelength, as shown in figure 11(*a*), is first selected. Using computer-assisted greyscale recognition and

https://doi.org/10.1017/jfm.2026.11512 Published online by Cambridge University Press

thresholding techniques, the original experimental image is converted into a binary image as presented in figure 11(*b*). The interface contour is identified from the binary image and is subsequently converted into physical coordinates, as illustrated in figure 11(*c*), thereby yielding a single-valued interface function $\eta = \eta(x)$ required for subsequent Fourier analysis, where x represents the spanwise coordinate.

(ii) Fourier analysis. The interface function $\eta = \eta(x)$ is decomposed using Fourier series expansion as

$$\eta(x) = c_0 + a \sum_{n=1}^{\infty} c_n \cos(nkx), \tag{B1}$$

where c_0 denotes the zeroth-order mode, representing the mean interface position, and the coefficients c_n correspond to the normalised amplitudes of higher-order perturbation modes. The coefficient c_0 is extracted for each image frame, from which the trajectory of the mean interface position and interface velocity jump Δu are obtained. For the interface contour shown in figure 11(*c*), the Fourier analysis yields c_0 with value 130.07 mm.

(iii) Bubble and spike amplitude determination. The bubble amplitude a_b and spike amplitude a_s are determined by subtracting the mean interface position c_0 from the streamwise coordinates of the bubble and spike tips, respectively.

(iv) Overall amplitude determination. Based on the obtained values of a_b and a_s, the overall interface amplitude can be determined as $a = (|a_b| + |a_s|)/2$.

It is noteworthy that the mean interface position obtained from Fourier analysis, corresponding to the unperturbed component with $k = 0$, is mathematically equivalent to the position defined by the equal bubble–spike volume criterion, i.e. the location where the area of the downstream bubble region equals that of the upstream spike region. The detailed derivation is presented below.

We define the interface profile at a given time as a function $\eta = \eta(x)$ over a single period $x \in [0, \lambda]$. The Fourier series of the interface function is given by (B1). The zeroth-order mode, denoted by c_0, naturally serves as a reference position because it defines the 'centreline' of the interface irrespective of higher-order modulations, and this definition has been widely adopted in previous studies (Zhou *et al.* 2021; Zhou 2024).

The position that separates the interface into equal bubble and spike volumes, y_0, is determined by the condition

$$\int_0^{\lambda} [\eta(x) - y_0] \, \mathrm{d}x = 0. \tag{B2}$$

Rearranging (B2) yields

$$y_0 = \frac{1}{\lambda} \int_0^{\lambda} \eta(x) \, \mathrm{d}x. \tag{B3}$$

By substituting (B1) into (B3) and integrating over an integer multiple of the period, the integral of $\cos(nkx)$ vanishes, resulting in

$$y_0 = \frac{1}{\lambda} \int_0^{\lambda} c_0 \, \mathrm{d}x = c_0. \tag{B4}$$

Therefore, the mean interface positions obtained from these two approaches are identical, and the choice between them does not affect the measured a_b and a_s.

https://doi.org/10.1017/jfm.2026.11512 Published online by Cambridge University Press

References

Abarzhi, S.I., Bhowmick, A.K., Naveh, A., Pandian, A., Swisher, N.C., Stellingwerf, R.F. & Arnett, W.D. 2019 Supernova, nuclear synthesis, fluid instabilities, and interfacial mixing. *Proc. Natl Acad. Sci. USA* **116**, 18184–18192.

Bakhrakh, S.M., Klopov, B.A., Meshkov, E.E., Tolshmyakov, A.I. & Yanikin, Y.V. 1995 Development of perturbations of a shock-accelerated interface between two gases. *J. Appl. Mech. Tech. Phys.* **36**, 341–346.

Brouillette, M. 2002 The Richtmyer–Meshkov instability. *Annu. Rev. Fluid Mech.* **34**, 445–468.

Cai, W., Jiang, S., Wang, H., Wang, P., Ma, D. & Si, T. 2025 Strong-shock-driven Richtmyer–Meshkov instability at a V-shaped interface. *Phys. Rev. Fluids* **10**, 104005.

Chen, C., Xing, Y., Wang, H., Zhai, Z. & Luo, X. 2023 Experimental study on Richtmyer–Meshkov instability at a light–heavy interface over a wide range of Atwood numbers. *J. Fluid Mech.* **975**, A29.

Chester, W. 1954 CXLV. The quasi-cylindrical shock tube. *Lond. Edin. Dublin Phil. Mag. J. Sci.* **45**, 1293.

Chisnell, R.F. 1957 The motion of a shock wave in a channel, with applications to cylindrical and spherical shock waves. *J. Fluid Mech.* **2**, 286–298.

Dimonte, G., Frerking, C.E., Schneider, M. & Remington, B. 1996 Richtmyer–Meshkov instability with strong radiatively driven shocks. *Phys. Plasmas* **3**, 614–630.

Dimonte, G., Nagori, M., Ramaprabhu, P. & Boureima, I. 2024 Simulations and models for the Richtmyer–Meshkov instability with broadband perturbations. *Phys. Fluids* **36** (2), 025143.

Dimonte, G. & Ramaprabhu, P. 2010 Simulations and model of the nonlinear Richtmyer–Meshkov instability. *Phys. Fluids* **22**, 014104.

Dimonte, G. & Remington, B. 1993 Richtmyer–Meshkov experiments on the Nova laser at high compression. *Phys. Rev. Lett.* **70**, 1806.

Dowse, J. & Skews, B. 2014 Area change effects on shock wave propagation. *Shock Waves* **24**, 365–373.

Glendinning S.G. *et al.* 2003 Effect of shock proximity on Richtmyer–Meshkov growth. *Phys. Plasmas* **10**, 1931–1936.

Guo, X., Cong, Z., Si, T. & Luo, X. 2022 Shock-tube studies of single- and quasi-single-mode perturbation growth in Richtmyer–Meshkov flows with reshock. *J. Fluid Mech.* **941**, A65.

Guo, X., Zhai, Z., Ding, J., Si, T. & Luo, X. 2020 Effects of transverse shock waves on early evolution of multi-mode chevron interface. *Phys. Fluids* **32**, 106101.

Guo, X., Zhai, Z., Si, T. & Luo, X. 2019 Bubble merger in initial Richtmyer–Meshkov instability on inverse-chevron interface. *Phys. Rev. Fluids* **4**, 092001.

Han, Z. & Yin, X. 1993 *Shock Dynamics: Fluid Mechanics and Its Application*. Kluwer Academic Publishers and Science Press.

Jiang, S., Cai, W., Xie, J., He, D., Wang, H., Si, T. & Luo, X. 2024 Realization of a shock-tube facility to study the Richtmyer–Meshkov instability driven by a strong shock wave. *Rev. Sci. Instrum.* **95**, 085114.

Li, J., Cao, Q., Wang, H., Zhai, Z. & Luo, X. 2023 New interface formation method for shock–interface interaction studies. *Exp. Fluids* **64**, 170.

Liang, Y., Zhai, Z., Ding, J. & Luo, X. 2019 Richtmyer–Meshkov instability on a quasi-single-mode interface. *J. Fluid Mech.* **872**, 729–751.

Lombardini, M. & Pullin, D.I. 2009 Startup process in the Richtmyer–Meshkov instability. *Phys. Fluids* **21**, 044104.

Luo, X., Dong, P., Si, T. & Zhai, Z. 2016 The Richtmyer–Meshkov instability of a 'V' shaped air/SF_6 interface. *J. Fluid Mech.* **802**, 186–202.

Meshkov, E.E. 1969 Instability of the interface of two gases accelerated by a shock wave. *Fluid Dyn.* **4**, 101–104.

Mikaelian, K.O. 1994 Freeze-out and the effect of compressibility in the Richtmyer–Meshkov instability. *Phys. Fluids* **6**, 356–368.

Mikaelian, K.O. 2005 Richtmyer–Meshkov instability of arbitrary shapes. *Phys. Fluids* **17**, 034101.

Mikaelian, K.O. 2016 Oscillations of a standing shock wave generated by the Richtmyer–Meshkov instability. *Phys. Rev. Fluids* **1**, 033601.

Mohaghar, M., Carter, J., Musci, B., Reilly, D., McFarland, J. & Ranjan, D. 2017 Evaluation of turbulent mixing transition in a shock-driven variable-density flow. *J. Fluid Mech.* **831**, 779–825.

Mohaghar, M., Carter, J., Pathikonda, G. & Ranjan, D. 2019 The transition to turbulence in shock-driven mixing: effects of Mach number and initial conditions. *J. Fluid Mech.* **871**, 595–635.

Napieralski, M., Cobos, F., Velikovich, A. & Huete, C. 2024 Richtmyer–Meshkov instability when a shock is reflected for fluids with arbitrary equation of state. *J. Fluid Mech.* **1000**, A18.

Ranjan, D., Anderson, M., Oakley, J. & Bonazza, R. 2005 Experimental investigation of a strongly shocked gas bubble. *Phys. Rev. Lett.* **94**, 184507.

https://doi.org/10.1017/jfm.2026.11512 Published online by Cambridge University Press

RANJAN, D., NIEDERHAUS, J., MOTL, B., ANDERSON, M., OAKLEY, J. & BONAZZA, R. 2007 Experimental investigation of primary and secondary features in high-Mach-number shock–bubble interaction. *Phys. Rev. Lett.* **98**, 024502.

REILLY, D., MCFARLAND, J., MOHAGHAR, M. & RANJAN, D. 2015 The effects of initial conditions and circulation deposition on the inclined-interface reshocked Richtmyer–Meshkov instability. *Exp. Fluids* **56**, 168.

RICHTMYER, R.D. 1960 Taylor instability in shock acceleration of compressible fluids. *Commun. Pure Appl. Maths* **13** (2), 297–319.

RIKANATI, A., ORON, D., SADOT, O. & SHVARTS, D. 2003 High initial amplitude and high Mach number effects on the evolution of the single-mode Richtmyer–Meshkov instability. *Phys. Rev. E* **67**, 026307.

RUSSELL, D.A. 1967 Shock-wave strengthening by area convergence. *J. Fluid Mech.* **27**, 305–314.

SADOT, O., RIKANATI, A., ORON, D., BEN-DOR, G. & SHVARTS, D. 2003 An experimental study of the high Mach number and high initial-amplitude effects on the evolution of the single-mode Richtmyer–Meshkov instability. *Laser Part. Beams* **21**, 341–346.

SI, T., JIANG, S., CAI, W., WANG, H., & LUO, X. 2025 Shock-tube experiments on strong-shock-driven single-mode Richtmyer–Meshkov instability. *J. Fluid Mech.* **1006**, R1.

WHITHAM, G.B. 1957 A new approach to problems of shock dynamics. Part I. Two-dimensional problems. *J. Fluid Mech.* **2**, 145–171.

WOUCHUK, J.G. 2001 Growth rate of the linear Richtmyer–Meshkov instability when a shock is reflected. *Phys. Rev. E* **63**, 056303.

YANG, Y., ZHANG, Q. & SHARP, D.H. 1994 Small amplitude theory of Richtmyer–Meshkov instability. *Phys. Fluids* **6**, 1856–1873.

ZHAI, Z., LIU, C., QIN, F., YANG, J. & LUO, X. 2010 Generation of cylindrical converging shock waves based on shock dynamics theory. *Phys. Fluids* **22**, 041701.

ZHAN, D., LI, Z., YANG, J., ZHU, Y. & YANG, J. 2018 Note: a contraction channel design for planar shock wave enhancement. *Rev. Sci. Instrum.* **89**, 056104.

ZHANG, Q. & GUO, W. 2016 Universality of finger growth in two-dimensional Rayleigh–Taylor and Richtmyer–Meshkov instabilities with all density ratios. *J. Fluid Mech.* **786**, 47–61.

ZHANG, Q. & SOHN, S.I. 1997 Nonlinear theory of unstable fluid mixing driven by shock wave. *Phys. Fluids* **9**, 1106.

ZHAO, Y., DING, J., HE, D., ZHOU, Z. & LUO, X. 2025 Convergent Richtmyer–Meshkov turbulence by time-resolved planar laser-induced fluorescence measurement. *J. Fluid Mech.* **1007**, A30.

ZHOU, Y. 2017*a* Rayleigh–Taylor and Richtmyer–Meshkov instability induced flow, turbulence, and mixing. I. *Phys. Rep.* **720–722**, 1–136.

ZHOU, Y. 2017*b* Rayleigh–Taylor and Richtmyer–Meshkov instability induced flow, turbulence, and mixing. II. *Phys. Rep.* **723–725**, 1–160.

ZHOU, Y. 2024 *Hydrodynamic Instabilities and Turbulence: Rayleigh–Taylor, Richtmyer–Meshkov, and Kelvin–Helmholtz Mixing*. Cambridge University Press.

ZHOU, Y., SADLER, J.D. & HURRICANE, O.A. 2025 Instabilities and mixing in inertial confinement fusion. *Annu. Rev. Fluid Mech.* **57**, 197–225.

ZHOU, Y. *et al.* 2021 Rayleigh–Taylor and Richtmyer–Meshkov instabilities: a journey through scales. *Physica D* **423**, 132838.

https://doi.org/10.1017/jfm.2026.11512 Published online by Cambridge University Press